# Predictions and Studies with a One-Dimensional Ice–Ocean Model

SHELLEY H. RIEDLINGER

*Naval Ocean Research and Development Activity, Stennis Space Center, Mississippi*

ALEX WARN-VARNAS

*Saclant Center, La Spezia, Italy*

(Manuscript received 30 January 1989, in final form 29 November 1989)

ABSTRACT

A coupled one-dimensional ice–ocean model is used for studies of Arctic phenomena. The ice–snow system is represented by the simplified thermodynamic ice model of Semtner and a dynamic approximation that neglects the internal stresses. The ocean is represented by the Mellor–Yamada level-2 turbulence mixed-layer model together with a prescribed geostrophic velocity.

The thermodynamic coupling considers an ice front and a salinity flux generated by the freezing or melting of ice. The dynamic coupling occurs via the turbulent stress that exists in the mixed layer beneath the ice. Various boundary conditions for ice–ocean coupling are examined including an analytical representation of the constant flux layer.

Two test cases are used for model validation and scientific studies. One is the standard climatological test used by Semtner and others. The other test case is with the AIDJEX data.

The ice–ocean model is compared to Semtner's ice model to determine the effects of a variable-depth mixed layer as opposed to an isothermal, fixed-depth mixed layer. In the variable-depth mixed layer model, a warm spot develops in the surface layers of the ocean during open water periods. When the ocean refreezes some heat remains in the warm spot and gradually diminishes as the ice continues to grow. This heat is released from the upper ocean through the mixing process. Its release significantly affects the heat budget and the growth rate of ice. Open water occurs nearly every year, in climatology simulations, as opposed to once every six years in the case Semtner examined.

Simulations of the AIDJEX Experiment predicted the general trends of the temperature and salinity measurements. Specific discrepancies may be due primarily to the omission of advection.

## 1. Introduction

Our work was motivated by the need to further develop and study the coupling of Arctic ice and ocean. The present status of the coupling ranges from an ocean described by prescribed heat fluxes and currents to an ocean coupled to the ice at various levels of sophistication.

Most of the previous ice models treated the ocean in a passive or a semipassive sense. The passive approach consisted of a prescription of climatological ocean currents and heat fluxes. The semipassive approach included a heat budget calculation with a constant depth mixed-layer prescription (Hibler 1980). Ocean climatologies ranged from mean annual to seasonal time scales. Examples are the work of Coachman and Aagaard (1974) for annual ocean currents or the diagnostic use of the Hibler–Bryan (1984) results for providing seasonally varying ocean currents and heat fluxes. In ice forecasting, the use of the seasonally varying ocean currents and heat fluxes has been shown to yield a more realistic ice edge (R. H. Preller, personal communication 1986).

Time-dependent thermodynamic models of sea ice, with and without snow, have been developed by Untersteiner (1964) and Maykut and Untersteiner (1971). The resultant numerical simulations, for thick ice, show realistic climatologies of temperature and ice thickness with a nearly isotropic summer temperature distribution changing to a strong gradient configuration in the winter indicative of a thermal front propagating from the surface.

The thermodynamic component of numerical ice–ocean models usually contains Semtner's (1976) snow and ice model. The simplest thermodynamic coupling to the ocean involves the prescription of a constant depth mixed layer and a heat budget calculation (Parkinson and Washington 1979; Hibler and Bryan 1984). More elaborate thermodynamic models have improved the representations of the polar mixed-layer region. Pollard et al. (1983), for example, have experimented with a bulk model superposed on a prescribed thermocline. The model was used to simulate the thermodynamic cycle of a snow, ice, and water system.

Lemke and Manley (1984) studied the seasonal

*Corresponding author address:* Ms. Shelley Riedlinger, NORDA Code 322, Stennis Space Center, Mississippi 35929-5004.

variation of the mixed layer and the pycnocline under polar sea ice with a bulk type model that predicted the mixed layer salinity, the mixed-layer depth, and the pycnocline thickness in the Beaufort Sea during AIDJEX. The results agreed with the seasonal trends of the data and indicated suitability for climatological simulations.

Later, this model was coupled to a thermodynamic sea ice model—Lemke (1987). Seasonal studies in the Arctic and Southern Ocean were performed with this model and showed the importance of variable mixed layer depth and oceanic heat flux.

Climatology simulations with the Semtner (1976) ice model can yield multiyear cycles of ice thickness followed by open water, a situation attributed to the insulating properties of snow. Ledley (1985) also investigated the problem and confirmed that the length and character of these cycles depend on the insulating properties of snow, the timing of the refreezing of new ice after open water periods, and the oceanic heat flux.

The simplest dynamic coupling of a snow, ice, and water system was accomplished through the use of a drag law between ice and ocean (Parkinson and Washington 1979; Hibler and Bryan 1984). A more detailed approach incorporates boundary layer formalism and uses an iteration technique to calculate the Reynolds stress between the ice and water (Overland et al. 1984).

Mellor et al. (1986) developed a time-dependent, second-moment, turbulence closure model of the coupled ice and ocean system. The model has a detailed boundary layer representation and considers freezing and melting phase transitions and represents the associated unstable and stable states. A molecular sublayer can also be included in this model.

Our approach considers a time-dependent, horizontally homogeneous snow, ice, and water system. The coupling of this system is developed on a stretched vertical grid. Second-order closure is used for the simulation of the polar mixed layer.

The thermodynamics of the ice and snow system utilizes the Semtner 0-layer model. The ice dynamics employs momentum equations that neglect the internal ice stresses. The coupling of the ice and polar mixed layer is developed through the interfacial stresses, heat fluxes, and freezing/melting processes representation. An analytical representation of the constant flux layer is built into the model. Other boundary conditions are also considered.

Studies of the climatological, seasonal, and daily cycles are performed with the coupled ice–ocean model. A previous climatological simulation of Semtner (1976) is repeated. Feedback due to ice–ocean coupling plays a role in these simulations. The effects of feedback can be seen in the multiyear equilibrium cycle of ice thickness, heat budget, surface temperature, and other variables.

The cycle of open-water appearance changes from Semtner's (1976) previous results. Sensitivity studies of the appearance and disappearance of open water are conducted with the coupled ice–ocean model by varying various parameters. During an open-water period, the water is heated by the incoming solar radiation. A warm spot develops and gradually diffuses as the water refreezes.

Another set of studies is performed with the AIDJEX data. The data spans a period of one year and contains daily measurements. Model simulations of the seasonal cycle are conducted with a time step that resolves the daily variations. The simulated conditions are compared with the AIDJEX data and show agreement with the trends of this data.

## 2. Description of the model

### a. *Introduction*

The thermodynamics of sea ice is represented by the Semtner (1976) 0-layer ice model that contains prognostic variables for snow thickness $H_s$, ice thickness $H_i$, and surface temperature $T_S$. The growth rate of ice is computed using an energy balance that contains the atmospheric forcing fluxes at the surface, steady conduction in the snow–ice system, and an oceanic flux at the bottom of the ice. Ice dynamics is incorporated into the ice–ocean model by considering the stresses generated by the winds and water and by ignoring the internal ice forces. The omitting of the internal ice forces is consistent with the one-dimensional approximation that neglects convergent and divergent motions.

The ice model is coupled to an ocean model, which consists of a diagnostically prescribed interior ocean via the geostrophic velocity and a mixed layer parameterization scheme based on Mellor–Yamada level-2 turbulence closure (Mellor and Yamada 1974). The geostrophic current is constant and assumed to be $-1.2$ cm s$^{-1}$ for the $x$-component $u_g$ and 0.65 cm s$^{-1}$ for the $y$-component $v_g$. The Ekman and inertial velocities are model simulated. Horizontal advection is not included. The temperature, salinity, density and velocity for the ocean model are defined at 17 vertical levels variably spaced from 2.5 m to 500 m. The vertical eddy fluxes are defined midway between each level. For more detail see Riedlinger and Warn-Varnas (1987).

### b. *Dynamic ice model*

The equations defining the ice drift are

$$\frac{\partial u_i}{\partial t} = f(v_i - v_g) + \frac{\tau_{ax}}{m} + \frac{\tau_{wx}}{m}, \tag{1}$$

$$\frac{\partial v_i}{\partial t} = -f(u_i - u_g) + \frac{\tau_{ay}}{m} + \frac{\tau_{wy}}{m}, \tag{2}$$

where $u_i$ and $v_i$ are the $x$- and $y$-components of the ice velocity, $\tau_{ax}$ and $\tau_{ay}$ are the $x$- and $y$-components of

the wind stress, $\tau_{wx}$ and $\tau_{wy}$ are the $x$- and $y$-component of the water stress, $f$ the Coriolis parameter, and $m$ is the mass per unit area of the ice.

### c. Ocean model

The conservation equations for temperature, salinity, and momentum in the ocean model are

$$\frac{\partial \bar{T}}{\partial t} = \frac{\partial}{\partial z}(-\overline{wT}) + \frac{\partial}{\partial z}(-\overline{w'T'}) - \frac{1}{\rho_0 c}\frac{\partial F_{SR}}{\partial z}, \quad (3)$$

$$\frac{\partial \bar{S}}{\partial t} = \frac{\partial}{\partial z}(-\overline{wS}) + \frac{\partial}{\partial z}(-\overline{w'S'}), \quad (4)$$

$$\frac{\partial \bar{u}_w}{\partial t} = f\bar{v}_w - f v_g + \frac{\partial}{\partial z}(-\overline{w'u'}), \quad (5)$$

$$\frac{\partial \bar{v}_w}{\partial t} = -f\bar{u}_w + f u_g + \frac{\partial}{\partial z}(-\overline{w'v'}), \quad (6)$$

where $T$ is temperature, $S$ salinity, $F_{SR}$ the incident solar radiation, $u_w$ and $v_w$ the $x$- and $y$-components of the current velocity, $w$ the $z$-component of the current velocity, $\rho_0$ a reference density for the ocean, $c$ the specific heat for the ocean, $t$ the time and $z$ the vertical coordinate. Ensemble means are denoted by $(\bar{})$, and primes indicate departure from these means.

The vertical velocity $w$ is a chosen constant, such that, $\overline{wT}$ at the bottom of the water column is a predetermined value.

The vertical eddy fluxes of temperature, salinity, and momentum are given by

$$\overline{w'T'} = -(K_H + \nu)\frac{\partial \bar{T}}{\partial z}, \quad (7)$$

$$\overline{w'S'} = -(K_H + \nu)\frac{\partial \bar{S}}{\partial z}, \quad (8)$$

$$\overline{w'u'} = -(K_M + \nu)\frac{\partial \bar{u}_w}{\partial z}, \quad (9)$$

$$\overline{w'v'} = -(K_M + \nu)\frac{\partial \bar{v}_w}{\partial z}, \quad (10)$$

where $K_H$ and $K_M$ are eddy diffusion coefficients and $\nu$ is a very weak "background" eddy diffusion that exists even below the mixed layer.

A certain amount of shortwave solar radiation can penetrate into the upper ocean, in the presence or absence of ice. At each depth level this radiation is expressed (unless otherwise stated) as

$$F_{SR} = F_{IS}e^{-0.00067z_k} \quad (11)$$

where $F_{IS}$ is the penetrating amount of solar radiation at the water interface, and $z_k$ is the depth level.

For a more detailed description of the ocean model equations see appendix A.

### d. Boundary conditions

The boundary conditions at the surface of the snow–ice are provided by the surface fluxes, $F_l$ latent heat, $F_t$ sensible heat, $F_L$ incoming longwave radiation and $F_R$ incoming shortwave radiation. These fluxes are used in the heat balance at the surface. The lower boundary condition consists of the ice remaining at the freezing point together with the jump condition across the ice-water front, $q_i \partial h_i/\partial t = F_S - F_B$ where $h_i$ is the ice thickness, $q_i$ is the heat of fusion for ice, $F_S$ the heat flux within the ice, and $F_B$ the oceanic heat flux.

The upper boundary conditions for the ocean depend on whether it is ice-covered or ice-free. When ice-covered, the boundary condition for temperature is the freezing point of the surface waters. The salinity boundary condition is dependent upon whether the ice is melting or freezing. It is assumed that when the ocean freezes all the salt is excluded from the ice, thus increasing the salinity of the surface layer. When the ice melts, fresh water is added to the surface layer. The salinity flux is then given by

$$(\overline{w'S'})_0 = \frac{\rho_i}{\rho_0}\frac{\Delta S}{1000}\frac{\partial h_i}{\partial t} + S_F \quad (12)$$

where $\rho_i$ is the density of ice, $\Delta S/1000$ is the salinity difference in ppt, assumed to be 30, $\partial h_i/\partial t$ is the change in the ice thickenss with time and $S_F$ is a constant freshwater influx equivalent to 720 kg m$^{-2}$ y$^{-1}$ (Pollard et al. 1983).

When there is no ice, the upper boundary conditions on the ocean for the temperature, salinity, and momentum equations are determined by the surface fluxes. These are

$$\left[-\overline{w'T'} + \nu\frac{\partial \bar{T}}{\partial z}\right]_{z=0} = \frac{(F_{SR} + F_t + F_l)}{\rho_0 c}, \quad (13)$$

$$\left[-\overline{w'S'} + \nu\frac{\partial \bar{S}}{\partial z}\right]_{z=0} = \frac{-F_l \bar{S}_0}{\rho_0} + S_F, \quad (14)$$

$$\left[-\overline{w'u'} + \nu\frac{\partial \bar{u}_w}{\partial z}\right]_{z=0} = \frac{\tau_{ax}}{\rho_0}, \quad (15)$$

$$\left[-\overline{w'v'} + \nu\frac{\partial \bar{v}_w}{\partial z}\right]_{z=0} = \frac{\tau_{ay}}{\rho_0}. \quad (16)$$

At the lower boundary the temperature, salinity, and momentum are held constant at the initial value.

The upper boundary condition for the ice velocity is given by the wind stresses. The stresses are computed using the drag law as

$$\frac{\tau_{ax}}{m} = 2.7 \times 10^{-3}\rho_a/(\rho_i h_i)(u_a^2 + v_a^2)^{1/2}u_a, \quad (17)$$

$$\frac{\tau_{ay}}{m} = 2.7 \times 10^{-3}\rho_a/(\rho_i h_i)(u_a^2 + v_a^2)^{1/2}v_a, \quad (18)$$

where $\rho_a$ is the density of air, and $u_a$ and $v_a$ are the $x$- and $y$-components of the wind.

Between the ice and ocean we have experimented with different sets of boundary conditions. One is the familiar drag law where the stresses are given by

$$\frac{\tau_{wx}}{m} = 5.5 \times 10^{-3}\rho_0/(\rho_i h_i)[(u_g - u_i)^2 + (v_g - v_i)^2]^{1/2}[(u_g - u_i)\cos 25° - (v_g - v_i)\sin 25°], \quad (19)$$

$$\frac{\tau_{wy}}{m} = 5.5 \times 10^{-3}\rho_0/(\rho_i h_i)[(u_g - u_i)^2 + (v_g - v_i)^2]^{1/2}[(v_g - v_i)\cos 25° + (u_g - u_i)\sin 25°]. \quad (20)$$

An angle of 25° is the value assumed for the turning angle between the ice and the water.

The other boundary conditions have an analytical representation of the constant flux layer built into them as follows:

$$\left\{\frac{\partial T}{\partial z}\right\}_{1/2} = \frac{T_1 - T_0}{z_{1/2}[\ln(z_1/z_{0T}) + kA_T]}, \quad (21)$$

$$\left\{\frac{\partial S}{\partial z}\right\}_{1/2} = \frac{S_1 - S_0}{z_{1/2}[\ln(z_1/z_{0S}) + kA_S]}, \quad (22)$$

$$\left\{\frac{\partial u}{\partial z}\right\}_{1/2} = \frac{u_1 - u_i}{z_{1/2}\ln(z_1/z_0)}, \quad (23)$$

$$\left\{\frac{\partial v}{\partial z}\right\}_{1/2} = \frac{v_1 - v_i}{z_{1/2}\ln(z_1/z_0)}, \quad (24)$$

where $A_T$ and $A_S$ represent the changes in temperature and salinity across the molecular sublayer. These terms are represented by the Yaglom and Kader (1974) approximations where $A_T = 3.14(\mathrm{Re})^{1/2}[(\mathrm{Pr})^{2/3} - 0.2] + 2.11$ and $A_S = 3.14(\mathrm{Re})^{1/2}[(\mathrm{Sc})^{2/3} - 0.2] + 2.11$. For sea water Pr = 13.8, Sc = 2432, and Re = $u_* z_0/\nu$ and is about 50 for $u_* = 0.01$ m s$^{-1}$. $T_1$, $S_1$, $u_1$ and $v_1$ are the corresponding values of temperature, salinity, and velocity at the first level in the ocean model. $T_0$ and $S_0$ are the temperature and salinity values at the roughness high for the ice. The values with the subscript ½ are at a point midway between the first level and the roughness height. We used $z_{0T} = 1.5$ cm, $z_{0S} = 1$ cm, and $z_0 = 3$ cm for the roughness heights for temperature, salinity, and momentum, respectively.

Furthermore,

$$(\overline{w'T'})_0 = K'_{H_{1/2}} z_{1/2}\left\{\frac{\partial T}{\partial z}\right\}_{1/2}. \quad (25)$$

Combining Eqs. (21) and (25) yields

$$(\overline{w'T'})_0 = K'_{H_{1/2}}\frac{T_1 - T_0}{[\ln(z_1/z_{0T}) + kA_T]}, \quad (26)$$

where $K'_{H_{1/2}} = K_{H_{1/2}}/z_{1/2}$ and $(\overline{w'T'})_0$ is the heat flux at the ice–ocean interface. A similar relation for salinity

$$(\overline{w'S'})_0 = K'_{H_{1/2}}\frac{S_1 - S_0}{[\ln(z_1/z_{0T}) + kA_T]}, \quad (27)$$

is used to determine $S_0$, the salinity at the roughness height. The actual salinity flux is computed using Eq. (12). The freezing temperature at the roughness height $T_0$ is obtained from the relationship $T_0 = mS_0$ where $m = -0.054$; Mellor et al. (1986).

The stress at the ice–ocean interface is calculated as

$$\tau_x = K'_{M_{1/2}}\frac{u_1 - u_i}{\ln(z_1/z_0)}, \quad (28)$$

$$\tau_y = K'_{M_{1/2}}\frac{v_1 - v_i}{\ln(z_1/z_0)}, \quad (29)$$

where $K'_{M_{1/2}} = K_{M_{1/2}}/z_{1/2}$. The eddy coefficients $K_{M_{1/2}}$ and $K_{H_{1/2}}$ are calculated with the use of the analytical representations Eqs. (21) through (24). This approach was suggested by Glyn Roberts (personal communication 1987).

### e. *Computing oceanic heat flux*

The heat flux from the ocean to the ice $F_B$ is calculated by considering the heat budget of the water column. Integrating Eq. (3) over the water column yields

$$F_B/\rho_0 c = \overline{w'T'}|_0 = \int_{z=0}^{z=z_1}\frac{\partial \bar{T}}{\partial z}\,dz + \overline{wT}|_{z_1} + \overline{w'T'}|_{z_1} + F_{SR}|_{z_1} - F_{SR}|_0. \quad (30)$$

Where the quantity $\overline{wT}|_{z_1}$ represents heat brought into the water column from the deep ocean, $\overline{w'T'}|_{z_1}$ represents the exchange of heat across the bottom boundary by diffusion, $[F_{SR}|_{z_1} - F_{SR}|_0]$ represents heating by solar radiation and $z_1$ is 500 m.

## 3. Climatological studies

### a. *Introduction*

We first considered one of the multiyear ice cycles simulated by Semtner (1976). In this example, all the ice melted every six years yielding an open-water period during the summer. In the fall the ice reappeared and grew rapidly through the following winter due to a thinner snow cover. We repeated this simulation with our coupled ice–ocean model in order to study the effects on ice thickness of a varying upper ocean and mixed layer heat budget. We will refer to Semtner's model as the constant mixed-layer model (CML) and ours as the variable mixed-layer model (VML).

In comparing the CML to the VML, we use as many of the same model parameters as possible. These parameters are listed in Table 1. The values for $H_i$ and $H_s$ are the initial ice thickness and snow thickness, re-

TABLE 1. Listing of parameters and assigned values used for some of the test cases.

| | Climatology | | AIDJEX | | |
|---|---|---|---|---|---|
| | Case 1 (CML) | Case 1 (VML) | Case 2 (VML) | Case 2J (VML) | Case 2Q (VML) |
| $H_i$ (m) | 0.50 | 0.50 | 3.40 | 3.40 | 3.40 |
| $H_s$ (m) | 0.30 | 0.30 | 0.30 | 0.20 | 0.30 |
| $F_B$ (W m$^{-2}$) | 8.07 | Variable | Variable | Variable | Variable |
| $H_{deep}$ (W m$^{-2}$) | None | 8.07 | 4.31 | 4.31 | 2.02 |
| $T_s$ (°C) | −2.0 | −2.0 | −2.0 | −2.0 | −2.0 |
| $T_B$ (°C) | −2.0 | Variable | Variable | Variable | Variable |
| $\sigma$ (W m$^{-2}$ K$^{-4}$) | $5.797 \times 10^{-8}$ | $5.797 \times 10^{-8}$ | $5.670 \times 10^{-8}$ | $5.670 \times 10^{-8}$ | $5.670 \times 10^{-8}$ |
| $\alpha_i$ | 0.66448 | 0.66448 | 0.64 | 0.64 | 0.64 |
| $\alpha_w$ | 0.07 | 0.07 | 0.07 | 0.07 | 0.07 |
| $q_s$ (MJ m$^{-3}$) | 302.0 | 302.0 | 302.0 | 302.0 | 302.0 |
| $q_b$ (MJ m$^{-3}$) | 268.0 | 268.0 | 302.0 | 302.0 | 302.0 |
| $\gamma$ | 1.065 | 1.065 | 1.0 | 1.0 | 1.0 |
| MLD (M) | 30.0 | Variable | Variable | Variable | Variable |
| Time step | 8 hours | 8 hours | 6 hours | 6 hours | 6 hours |
| Heat fluxes | Climatology | Climatology | AIDJEX data | AIDJEX data | AIDJEX data |
| Winds | None | FNOC data | AIDJEX data | AIDJEX data | AIDJEX data |
| Initial $T$ and $S$ | None | AIDJEX data | AIDJEX data | AIDJEX data | AIDJEX data |

spectively. The heat flux from the ocean to the ice, $F_B$, is a constant −8.07 W m$^{-2}$ in the CML. In the VML, $F_B$ is determined from the change in the heat content of the water column, Eq. (30) in section 2e. The heat flux from the deep ocean $wT|_{z_1}$, denoted by $H_{deep}$, is a constant in the VML and is given the value of −8.07 W m$^{-2}$. In the CML, $F_B$ and $H_{deep}$ are the same thing. The surface temperature $T_S$ is set initially to −2°C in both models. The temperature at the bottom of the ice $T_B$ is assumed to always be at the freezing point of the surface water. In the CML, this value is −2°C. In the VML, the freezing point varies with the salinity of the mixed layer. The Stefan–Boltzmann constant $\sigma$ is about 2% higher than the standard value. Semtner used this value to compare his results with Maykut and Untersteiner (1969). The value given for $\alpha_i$ is used in the 0-layer ice model to account for some of the solar radiation that penetrates into snow-free ice (Appendix, Semtner 1976). The quantities $q_s$ and $q_b$ are the volumetric heats of fusion at the top and bottom of the ice. Gamma is a correction factor Semtner used, since the 0-layer ice model does not keep track of solar radiation stored in the ice in brine pockets. He increased the snow and ice conductivities by the factor 1.065. The mixed-layer depth MLD was 30 m in the CML. In the VML, this quantity is determined by the dynamics of the mixed layer.

Both models were forced with incoming shortwave radiation, incoming longwave radiation, sensible heat, latent heat, and albedo values obtained from Fletcher's monthly mean climatology (Table 1, Semtner 1976). Semtner's snowfall rate was also used. For the VML model average, monthly winds from the 1983 Fleet Numerical Oceanography Center (FNOC) analysis were used for the wind forcing and the ocean temperature and salinity values were initialized using profiles taken from AIDJEX data at station Blue Fox 1 January 1976 (Fig. 1). These profiles represent typical winter profiles for the Beaufort Sea. The drag law is used as the boundary condition for the winds on the ice and for the ice on the ocean interface.

### b. *Comparing model results*

Each model was integrated for 20 years. The ice thickness and ice plus snow thickness values for both cases are shown in Fig. 2. The top graph in this figure is the CML case. The bottom graph is the VML case.

A six-year, no-ice cycle, such as the one obtained by Semtner, quickly develops in the CML simulation. In the VML simulation, a short open-water period occurs during year 2 and again in year 4. Then beginning in year 6, open water occurs every year, with the length of the open-water period increasing each successive year. The no-ice cycles for these cases are obviously quite different.

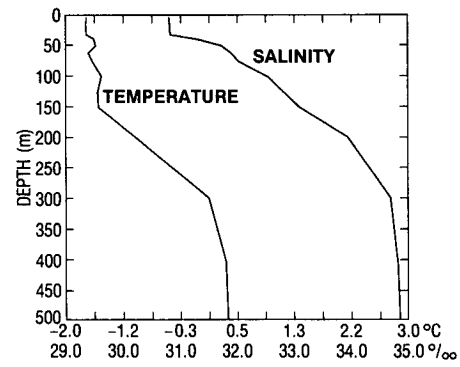


FIG. 1. Temperature and salinity profiles from Station Blue Fox, 1 January 1976. These profiles were used to initialize the ice–ocean model for the climatology test cases.

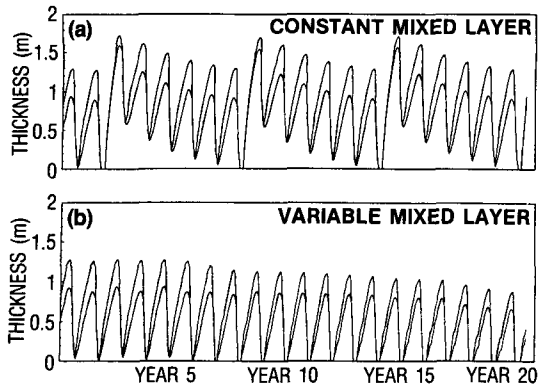


FIG. 2. The yearly variability of the ice and ice plus snow thickness for a 20-year simulation of the CML model (a) and the VML model (b).

In the CML case, the open-water temperature is computed using a constant mixed-layer depth. The water temperature increases to a maximum of −1.002°C during the open-water period and then decreases back to a −2.0°C value before ice is reformed. When the ocean is ice covered, the water temperature remains near the freezing point. This pattern changes little throughout the simulation.

The length of each open-water period is fairly constant. The average open-water period during the simulation is 54.7 days. Each year in which open water occurs, the ice cover disappears in late August (around 20 August) and reforms in mid-October (around 15 October). The heaviest snowfall in the simulation occurs during the months of September and October. Thus, open water exists during the time when the snowfall is the greatest, resulting in a thin snow cover the year following an open-water period. Snow cover acts as an insulator slowing down the growth of ice. With a very thin snow cover this insulating effect is greatly reduced, and ice growth is quite rapid. From Fig. 2, it is seen that the ice thickness is the greatest in the year following an open-water event. The ice thins each successive year until open water occurs again. The snow cover during these years is thicker than in the year following the open-water event. The thicker snow cover insulates the ice from the surface fluxes and slows down the freezing rate. In addition, the constant oceanic heat flux gradually reduces the ice thickness by melting at the bottom. A similar effect due to snow cover was observed by Ledley (1985) in her study of the multiyear cycles using Semtner's model.

In the VML simulation, the mixed layer interacts with the ice or the atmosphere every time step. The heat, salt, and momentum fluxes control heating and mixing within the water column. Heating and mixing within the water column affects the growth and decay of the ice. This primary difference in the simulations shows up in the second year for the VML. In this year, a short open-water period (4.7 days) occurs. The mixed layer is shallow, 2.5 m as opposed to 30 m in the CML and reacts quickly with atmospheric forces losing heat and refreezing. (The mixed-layer depth is defined as the maximum depth at which the salinity has changed by no more than 0.1 ppt from its surface value.) Ice now exists during the heavy snowfall months. A thick snow cover soon forms, which insulates the ice and slows down the freezing rate. The ice thickness in year 3 in the VML case is much thinner than year 3 in the CML case (a maximum of 0.94 m as opposed to 1.60 m). The decrease in ice growth eventually results in more frequent and longer open-water periods. By year 20, open water lasts for 80 days.

Snow cover is not, however, the only factor in the thinner ice and shorter open-water period that occurs in year 2. The oceanic heat flux is also important. Table 2 is a listing of several values computed by the model and includes the amount of heat input into the water column from the deep ocean, from diffusion, and from solar heating. The heat input from the deep ocean and from diffusion vary little from year to year. A large variability occurs in the solar heating term. This results in variability of the oceanic heat flux and the net heating of the water column. Each depth level in the ocean model absorbs different amounts of heat from solar radiation. The surface level (2.5-m level) absorbs the most solar heat. It can also lose heat more quickly than the deeper layers due to the combined effects of surface forcing and mixing. As an example, the maximum temperature that occurs in the water column in the year following the open-water period is −1.381°C, and it occurs at the 12.5 m depth level.

When ice reforms, the surface waters are at the freezing point, but the subsurface waters are slightly above freezing. This heat in the subsurface waters is released as the ice continues to grow and the mixed layer deepens. The release of this heat during the growth of ice slows down the freezing rate and yields thinner ice. This in combination with the snow cover, explains why years 2 and 3 are so different between the CML and VML simulations. These effects accumulate year after year gradually warming the upper ocean and thinning the ice cover. The maximum temperature at the 2.5 m depth level increases from −1.625°C in year 3 to 0.672°C in year 20. Similarly, the mean ice thickness decreases from 0.53 m in year 3 to 0.30 m in year 20.

Using year 10, as an example, the heating of the water column will be examined further. The open-water period for this year lasted 38.3 days. It opened on 10 August and refroze on 20 September. This period is not 38.3 consecutive days of open water, but 36 days of open water followed by a brief period of ice growth between 16 September and 18 September. During this time 2 cm of ice formed. The mixed layer deepened as a result of the ice growth and in the process released some heat from below the mixed layer. The heat was sufficient to melt the thin ice cover. The ocean re-

TABLE 2. Listing of number of open-water days, ice thicknesses, mixed-layer temperatures, and oceanic heating (MJ $m^{-2}$ $yr^{-1}$) for a 20-year simulation of the VML model (Case 1).

Variable Mixed Layer–Case 1

| Year | Number of open water days | Mean annual ice thickness (m) | $T(1)$ max (°C) | $T$ max (°C) | $H_{deep}$ | Diff | Solar | $F_B$ | Net |
|---|---|---|---|---|---|---|---|---|---|
| 1 | 0.0 | 0.517 | −1.611 | −1.460 | 251.1 | 10.8 | 0.0 | −259.2 | 2.7 |
| 2 | 4.7 | 0.501 | −1.546 | −1.381 | 251.1 | 13.2 | 41.1 | −293.2 | 12.1 |
| 3 | 0.0 | 0.533 | −1.625 | −1.449 | 251.1 | 15.0 | 0.0 | −263.4 | 2.7 |
| 4 | 4.3 | 0.504 | −1.555 | −1.408 | 251.0 | 16.4 | 37.7 | −294.1 | 11.1 |
| 5 | 0.0 | 0.531 | −1.632 | −1.397 | 251.0 | 17.6 | 0.0 | −265.3 | 3.3 |
| 6 | 9.3 | 0.486 | −1.572 | −1.105 | 251.0 | 18.4 | 85.4 | −330.0 | 24.9 |
| 7 | 24.0 | 0.463 | −1.391 | −0.546 | 251.0 | 19.1 | 208.8 | −437.6 | 41.3 |
| 8 | 40.0 | 0.437 | −0.976 | −0.123 | 251.0 | 19.6 | 332.8 | −559.6 | 43.8 |
| 9 | 35.7 | 0.453 | −1.090 | −0.224 | 251.0 | 20.0 | 300.4 | −548.5 | 22.9 |
| 10 | 38.3 | 0.447 | −1.020 | −0.156 | 251.0 | 20.1 | 320.2 | −566.2 | 25.3 |
| 11 | 41.3 | 0.438 | −0.924 | −0.065 | 251.0 | 20.5 | 344.0 | −589.5 | 26.0 |
| 12 | 43.0 | 0.431 | −0.850 | 0.005 | 251.0 | 20.6 | 359.6 | −606.2 | 25.0 |
| 13 | 46.7 | 0.421 | −0.724 | 0.123 | 251.0 | 20.6 | 389.1 | −634.0 | 26.7 |
| 14 | 49.0 | 0.414 | −0.619 | 0.221 | 251.0 | 20.5 | 410.5 | −655.5 | 26.6 |
| 15 | 52.3 | 0.400 | −0.463 | 0.363 | 251.0 | 20.5 | 442.6 | −687.3 | 26.8 |
| 16 | 54.3 | 0.390 | −0.353 | 0.464 | 251.0 | 20.3 | 463.5 | −708.9 | 26.0 |
| 17 | 53.0 | 0.377 | −0.298 | 0.517 | 251.0 | 20.2 | 467.7 | −704.8 | 34.0 |
| 18 | 62.0 | 0.331 | 0.161 | 0.946 | 251.0 | 20.0 | 558.7 | −776.6 | 53.1 |
| 19 | 67.3 | 0.306 | 0.458 | 1.227 | 251.0 | 19.7 | 616.7 | −836.3 | 51.2 |
| 20 | 80.7 | 0.300 | 0.672 | 1.431 | 251.0 | 19.5 | 673.0 | −936.6 | 6.9 |

$T(1)$ max = Maximum Temperature at Depth Level 1 (2.5 M).
$T$ max = Maximum Temperature at any Depth in the Water Column.
$H_{deep}$ = Total Heat Input into the Water Column by Advection From the Deep Ocean.
Diff = Total Heat Input into the Water Column by Diffusion Across the Bottom.
Solar = Total Heat Input into the Water Column by Solar Radiation.
$F_B$ = Total Heat Transfer Across the Ice–Ocean or Air–Ocean Interface.
Net = $H_{deep}$ + Diff + Solar + $F_B$.

mained ice-free until 20 September when continuous ice growth began.

Temperature profile plots for this year are shown in Fig. 3. Corresponding salinity profiles are shown in Fig. 4. At step 655 (9 August) in the figure, no warm region is observed in the water column down to 100 m. At step 680 (17 August), a warm spot begins to form and grows until step 780 (20 September), (open water exists from step 659 to step 780). After this step, the warm spot is seen to decrease at the same time the mixed layer deepens. However, not all the heat in the warm spot is exhausted by the end of the year. In fact, it is not until early spring of the following year that the warm spot disappears. Thus, the heat input into the water column during this open-water period affects the growth of ice for several months after ice reforms. The net result is thinner ice and warmer water below the ice. In general, the heat input into the water column in a year's time is not all released in that year. Examining Table 2, one sees that the net heating is always positive and fluctuates from year to year.

### c. *Oceanic heat flux*

The variability of the oceanic heat flux is shown in Fig. 5 along with the mixed-layer depth and ice thickness for years 6–10. The oceanic heat flux during the growth of ice in the fall and winter is frequently much larger than the deep-ocean heat value of −8.07 W $m^{-2}$. The only time $F_B$ stays near this value is in the summer when ice is melting and the mixed layer is shallowing.

Comparing the oceanic heat flux plot (Fig. 5a) to the plot of the salinity mixed-layer depth (Fig. 5b), one sees that these large oceanic heat flux values are a result of the release of heat stored in the water column by the deepening of the mixed layer. The heat is released in bursts that can be quite large.

The deepening of the mixed layer is controlled by convection due to density instabilities and vertical shears generated by the relative motion of the ice and ocean. When ice is growing, the salinity and density of the surface layers increase. Eventually the density structure becomes unstable and mixing occurs. If warmer water exists below the mixed layer, the heat in this water raises the temperature of the mixed layer. This heat can then either slow down the freezing rate or melt a few centimeters of ice. The rate at which the heat is released depends strongly on mechanical mixing.

The way in which one defines the mixed layer is important in understanding this situation. Earlier, we defined the mixed layer as the region where the salinity has not changed by more than 0.1 ppt from the surface value. (The density will change very little in the region

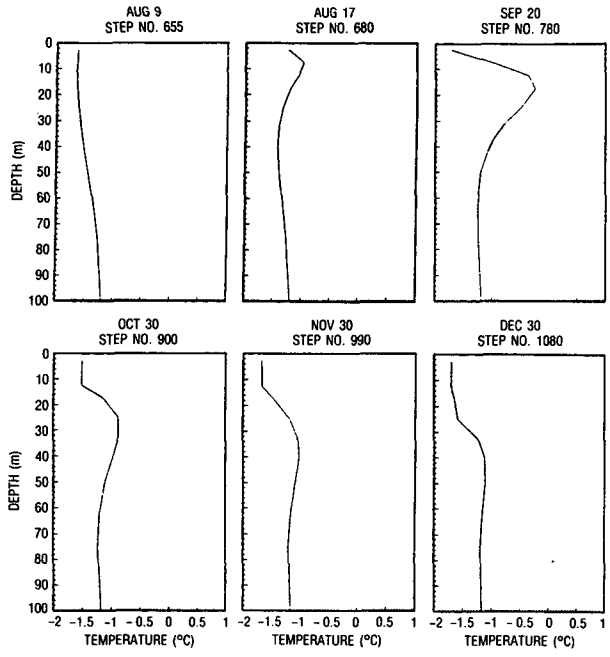


FIG. 3. Temperature profile plots from the VML simulation. These profiles show conditions before, during, and after the open-water period in year 10 of the simulation. Open water exists from step 659 to step 780.

also.) However, the temperature may increase toward the bottom of the region; e.g., the salinity increases from 31.07 ppt at 2.5 m to 31.17 ppt at 25 m (the mixed-layer depth by our definition). The temperature increases from −1.68° to −0.96°C in the same region (see Table 3). The heat at the bottom of the region will eventually be transferred to the surface and affect the formation of ice. If the winds and ice motion are fairly calm, the primary method of transferring heat will be diffusion. If, on the other hand, the winds and ice motion are brisk, mechanical mixing in this region will be significant due to the uniform density structure. The transfer of heat to the surface will occur more quickly. This is the reason for the spikes observed in the heat flux plot in Fig. 5a.

## 4. Case 2—AIDJEX simulations

### a. Introduction

We decided to attempt to model some of the changes observed in an Arctic experiment in order to test the model's representation of physical processes and its predictive ability of measured quantities. We obtained the AIDJEX data and performed simulations of this experiment with our ice–ocean model. The following forcing fields are required as model input: incoming solar radiation, incoming longwave radiation, latent heat flux, sensible heat flux, albedo, winds, snowfall rates, and the heat flux from the deep ocean. The model also needs the initial values for the ice thickness, snow thickness, and the temperature and salinity profiles in the ocean. Most of the meteorological forcing data was obtained from two AIDJEX reports. The first is *Report on the AIDJEX Meteorological Experiment* (Leavitt et al. 1978). From this report, the latent and sensible heat fluxes, the average air temperature, and the wind speed and direction were obtained. The second report is *Radiation Program during AIDJEX: A Data Report* (Pautzke and Hornof 1978). This report gives the daily total of the incoming solar radiation and the daily average for the albedo. All the forcing values are averaged between the four camps to get an average forcing for the region. The incoming longwave radiation is not given directly in the AIDJEX data but can be computed from the average air temperature with the method used in Parkinson and Washington (1979). The initial ice thickness and the initial temperature and salinity profiles can be obtained from AIDJEX technical reports. Ice thickness measurements were made at the beginning of the experiment. These values ranged from 2.5 to 4.7 m at the four camps: the average thickness was 3.4 m. This value was used to initialize the model. The snowfall rates and the deep ocean heat flux were not given in any of the AIDJEX reports. Therefore, the climatology values used in the previous model simulations were used here.

The AIDJEX data runs from 1 May 1975 to 29 April 1976. All fluxes except the albedo and solar radiation are given at 6-hour intervals. Thus, the time step for

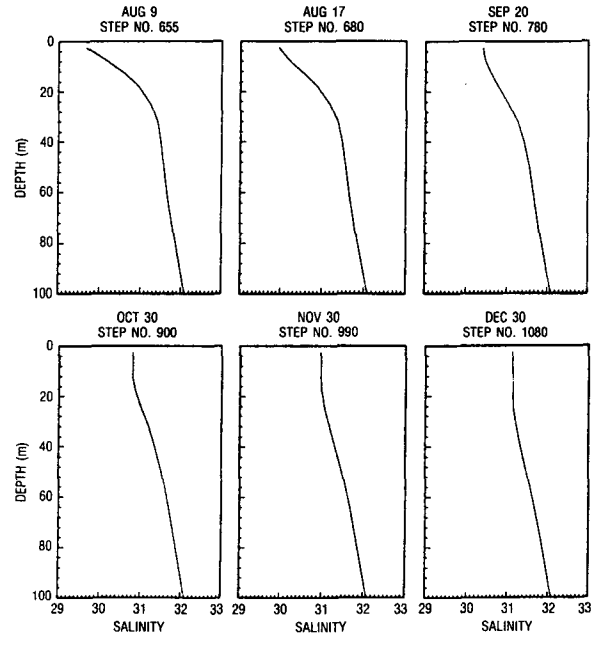


FIG. 4. Salinity profile plots from the VML simulation. These profiles show conditions before, during, and after the open-water period in year 10 of the simulation. Open water exists from step 659 to step 780.

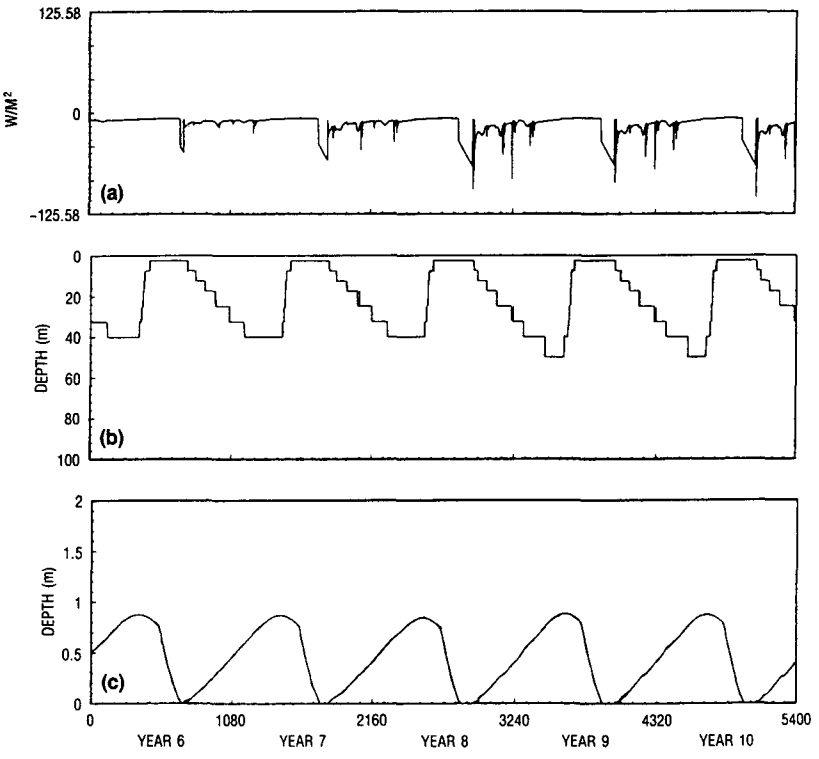


FIG. 5. (a) Plots of the oceanic heat flux, (b) the salinity mixed-layer depth, and (c) the ice thickness for years 6–10 of the VML simulation.

the AIDJEX simulations was 6 hours. The solar radiation in the report is a daily total, so the solar radiation was partitioned into 6-hour intervals as the other data using the formulation as follows.

Most of the input data is given at 0, 6, 12 and 18 hours UTC. Local time is about 10 hours earlier, thus the first period in the model simulation is from 1400 to 2000, the second period is from 2000 to 0200, the third period is from 0200 to 0800 and the fourth period is from 0800 to 1400. The first and fourth periods are daytime hours, and the second and third periods are nighttime hours. It is further assumed that the maximum solar radiation influx occurs during the fourth period, i.e., the 0800 to 1400 interval.

The year is divided into four groups. The first group is summer, i.e. the months of May, June and July.

TABLE 3. Example of mixed-layer temperature and salinity structure in the VML model for Case 1.

| Depth (m) | Temperature (°C) | Salinity (ppt) | Sigma-*t* |
|---|---|---|---|
| 2.5 | −1.685 | 31.068 | 25.011 |
| 7.5 | −1.685 | 31.067 | 25.010 |
| 12.5 | −1.684 | 31.067 | 25.010 |
| 17.5 | −1.492 | 31.084 | 25.020 |
| 25.0 | −0.962 | 31.168 | 25.073 |
| 32.5 | −0.745 | 31.280 | 25.156 |

During these months some solar radiation exists at each time period. In particular, 30% of the daily total of solar radiation is assumed to arrive during the first period, 10% during each of the next two periods (the nighttime hours), and 50% during the last period. The second group is the fall and spring months of August, September, March and April. During these months no solar radiation arrives during the nighttime hours. The total solar radiation for the day is divided between the daytime hours: 30% for one, 70% for the other. The third group includes the months of October and February. For these months, solar radiation exists during only one of the daytime periods. The rest of the time the solar radiation is zero. The last group is the winter months of November, December and January, when the solar radiation is zero throughout the day. This partitioning was deduced from Fig. 10 in the report by Pautzke and Hornof.

The time series that results when the above partitioning is applied to the solar radiation data is quite variable, with most of the energy being concentrated during daytime hours and little or none existing during nighttime hours (Riedlinger and Warn-Varnas 1987).

### *b. Model results versus AIDJEX data*

A one-year simulation of the AIDJEX Experiment is performed with the ice-ocean model. The atmo-

spheric forcing is derived from AIDJEX data as described in the previous section. The initial temperature and salinity profiles are from 10 May 1975, Station Blue Fox. Values of $5.67 \times 10^{-8}$ W m$^{-2}$ K$^{-4}$ for $\sigma$ and $302 \times 10^{6}$ J m$^{-3}$ for $q_b$ are used in this test case. Sensitivity studies with the climatology test case (Riedlinger and Warn-Varnas 1987) showed that these values result in thinner ice. A value of 4.31 W m$^{-2}$ was used for $H_{\text{deep}}$. Other parameter values are listed in Table 1. The results of the simulation are compared with AIDJEX data.

Comparisons are made on how well the model simulates the mixed-layer characteristics rather than the growth and decay of ice. Considerable data exist as to the temperature and salinity structure in the water column below the ice during AIDJEX but very little on the ice thickness and ice growth and decay.

The mixed-layer salinity simulated by the model for one year, along with the mixed-layer salinity at Station Snowbird and Station Blue Fox, are shown in Fig. 6. The model simulates the trends of salinity well. In the winter and early spring, however, the salinity is a little too fresh. The mixed-layer depth determined from the salinity (as described earlier in this paper) is plotted in Fig. 7. The model again follows the general trends quite well. It causes shallowing of the mixed layer in the summer and deepening in the winter. The model, however, shallows too much in the summer and underestimates the mixed-layer deepening in the winter.

The simulated mixed-layer temperature followed the freezing temperature of salt water with a slight increase in the summer, followed by a decrease in the fall. The data showed more variability and slightly greater magnitudes.

The discrepancies between the simulated results and data may be due to several factors. The turbulence parameters prescribed in the model may need to be tuned to cause the mixed layer to deepen more. They may also be due to uncertainties in some of the forcing values used in the model, for example, the snowfall rate and the heat flux from the deep ocean. Or they may be due to advection, which is not accounted for in the model. Some of these possibilities will be examined later.

A comparison of temperature and salinity profiles from the model simulation with data at Station Blue Fox is shown in Figs. 8 and 9. The solid line in the plots is the model-determined profile and the dashed line is from AIDJEX data. Again the general trends

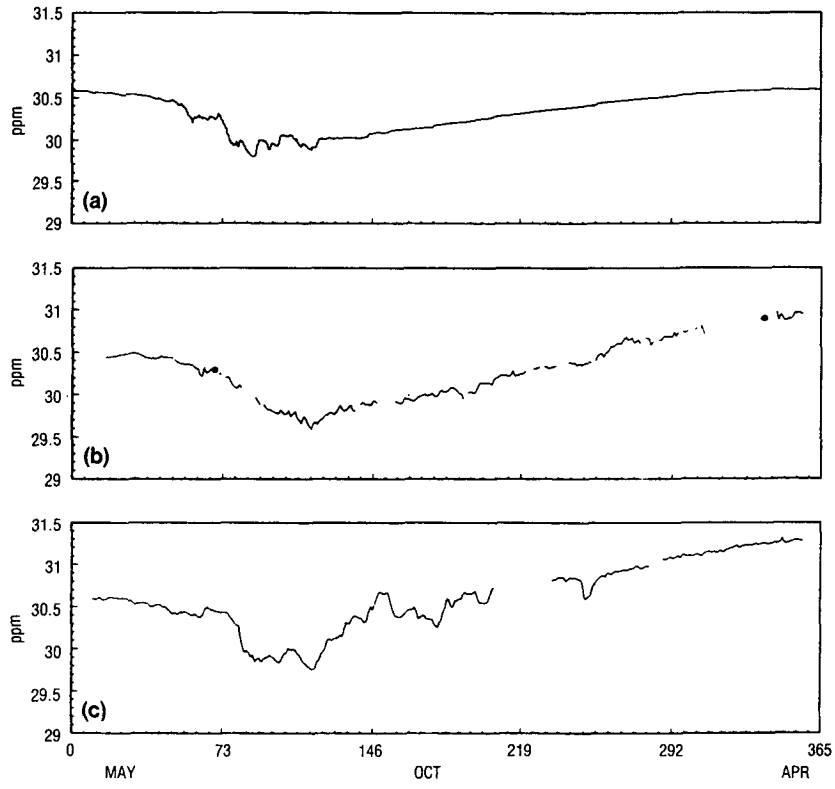


FIG. 6. (a) Mixed-layer salinity for a 1-year simulation of the VML forced with AIDJEX forcing data. Simulation runs from 1 May to 29 April, (b) mixed-layer salinity measured at camp Snowbird from 10 May 1975 to 20 April 1976, (c) mixed-layer salinity measured at camp Blue Fox from 10 May 1975 to 20 April 1975 (data is one value per day).

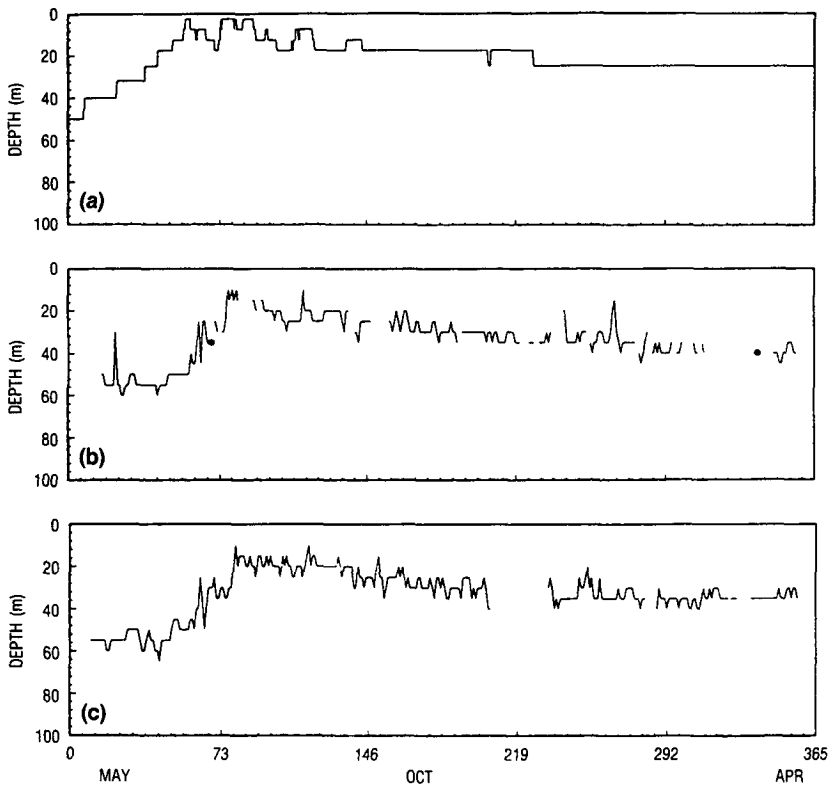


FIG. 7. (a) Mixed-layer depth for a 1-year simulation of the VML model forced with AIDJEX forcing data. Simulation runs from 1 May to 29 April, (b) mixed-layer depth measured at camp Snowbird from 10 May 1975 to 20 April 1976, (c) mixed-layer depth measured at camp Blue Fox from 10 May 1975 to 20 April 1975 (data is one value per day).

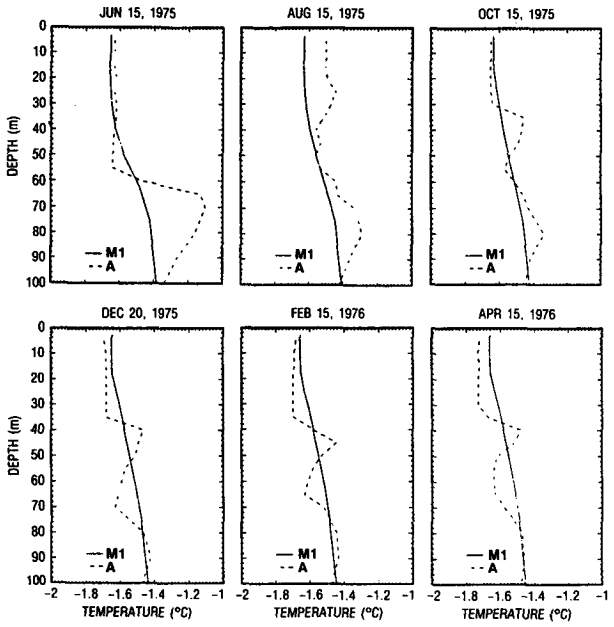


FIG. 8. Comparison of temperature profiles from AIDJEX case (solid line) and camp Blue Fox (dashed line).

and magnitudes compare well, except the mixed layer is too shallow and the profiles from the data show more variability. In summer, in the upper 30–50 m, the data shows a warmer ocean than the model profiles. In winter, the temperature of the upper ocean is somewhat cooler in the data than in the model simulations. The salinity profiles compare better, except that they tend to be a little fresher in the model profiles than in the data profiles. Maximums and minimums for the mixed-layer temperature, salinity, and mixed-layer depth for the four AIDJEX camps and for several model runs with AIDJEX data are shown in Table 4.

In the depth range of 50–100 m, the temperature profiles from the model are in rough agreement with the data, but the model does not indicate the temperature maximum around 70 m depth, which is quite apparent at Blue Fox in the summer. This temperature maximum is attributed to Pacific water, which enters the Arctic through the Bering Strait, eventually flows into the Beaufort Sea, and shows up in the data from 50 to 130 m depth. Also, several eddies were observed during the AIDJEX experiment. These eddies were located from 50 to 300 m depth. Thus, advection can be expected to be important in simulating the temperature

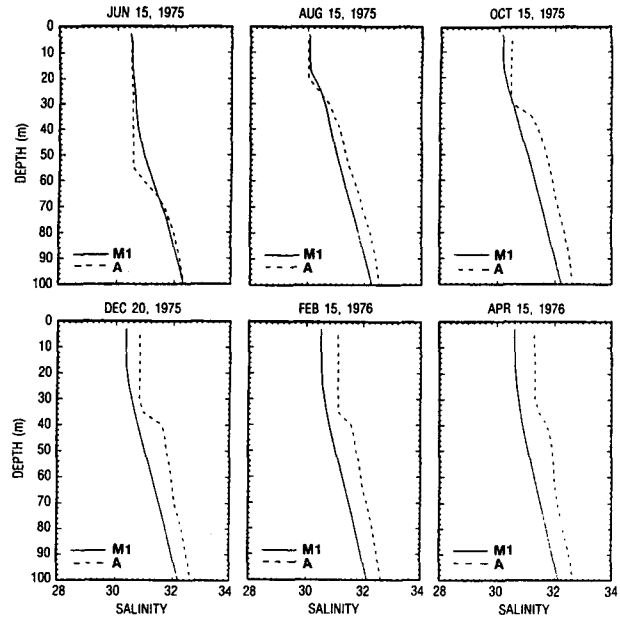


FIG. 9. Comparison of salinity profiles from AIDJEX case (solid line) and camp Blue Fox (dashed line).

and salinity structures in the Beaufort Sea and probably accounts for some of the differences between model results and data.

As mentioned earlier, uncertainties in some of the forcing fluxes may also account for some of the discrepancies in the temperature and salinity fields. We examined the snowfall rate and the heat flux from the deep ocean. To test how the snow cover might affect the ocean under the ice, the snowfall rate was reduced by one-half and the initial snow thickness value was decreased to 0.2 m. The result of this test case (Case 2J; Table 4) was an increase in the growth of ice in the winter and less melting in the summer. About 0.1 m more ice grew in the winter in this case than in the previous case and the mixed layer deepened to 32 m instead of 25 m in the winter. Similar results occurred when the heat flux from the deep ocean was reduced to 2.02 W $m^{-2}$ (Case 2Q; Table 4). Both changes increased the growth of ice in the winter, which resulted in increased salinity flux at the surface and increased deepening of the mixed layer.

## 5. Boundary condition studies at the ice–ocean interface

We have incorporated an analytical representation of the constant flux layer with and without a molecular sublayer as outlined in section 2d. This introduces a more detailed parameterization of boundary layer physics. These boundary conditions are compared with the previous approach which used a drag law formalism for the momentum equations.

The grid spacing for the analytical constant flux-layer representation had to be changed, since the simulated water speed was influenced by it. The first grid point must be closer to the ice–ocean interface than

TABLE 4. Listing of maximums and minimums in temperature, salinity, and mixed-layer depth for the four camps of AIDJEX and several VML model runs.

| | Mixed-layer characteristics | | | | | | | |
|---|---|---|---|---|---|---|---|---|
| | Bluefox | | Snowbird | | Big Bear | | Caribou | |
| | Max | Min | Max | Min | Max | Min | Max | Min |
| Temperature (°C) | −1.20 | −1.73 | −1.44 | −1.78 | −1.46 | −1.17 | −1.40 | −1.76 |
| Salinity (ppt) | 31.32 | 29.77 | 30.98 | 29.59 | 31.17 | 29.76 | 30.48 | 29.79 |
| Depth (m) | 65.0 | 10.0 | 60.0 | 10.0 | 60.0 | 15.0 | 60.0 | 15.0 |
| | AIDJEX-Case 2 | | AIDJEX-Case 2J | | AIDJEX-Case 2Q | | | |
| | Max | Min | Max | Min | Max | Min | | |
| Temperature (°C) | −1.62 | −1.66 | −1.61 | −1.66 | −1.62 | −1.67 | | |
| Salinity (ppt) | 30.60 | 29.79 | 30.67 | 29.76 | 30.74 | 29.88 | | |
| Depth (m) | 50.0 | 2.5 | 50.0 | 2.5 | 50.0 | 2.5 | | |
| | AIDJEX-CFL | | AIDJEX-Sublayer | | AIDJEX-Drag law | | | |
| | Max | Min | Max | Min | Max | Min | | |
| Temperature (°C) | −1.59 | −1.66 | −1.52 | −1.66 | −1.60 | −1.66 | | |
| Salinity (ppt) | 30.59 | 29.43 | 30.59 | 29.36 | 30.58 | 29.61 | | |
| Depth (m) | 25.0 | 0.3 | 25.0 | 0.3 | 25.0 | 0.3 | | |

2.5 m. We kept 17 depth levels and the last 8 levels were unchanged from the previous simulations. The upper 9 levels were changed to 0.3, 1.2, 2.5, 5.0, 9.0, 15.0, 25.0, 40.0 and 55.0 m.

We chose the AIDJEX simulation for our study because of the availability of data against which we can compare the simulated results with the various boundary conditions. The simulations were run for one year.

The simulated temperature and salinity at the first depth level, and some of the data are shown in Figs. 10 and 11. Figure 10a represents the temperature below the ice simulated with a constant flux layer without the molecular sublayer. Curve b in the same figure depicts the case with a molecular sublayer added to the constant flux layer. Curve c shows the data at Station Snowbird. As indicated, the data show more variability than either simulation. The results with the molecular sublayer emulate the data more closely. The salinity simulations in Fig. 11 include a case where the drag law is used for interface with the ice and ocean, curve a. In this figure, curves b and c are similar and different from curve a. The introduction of the constant flux and molecular sublayers shows more variability in mixed-layer salinity. The data shown in Fig. 11 indicate variability about the general winter and summer trend. The temperature and salinity maximums and minimums are shown in Table 4. Mixed-layer depth plots for these cases are not shown but they are similar to the one shown in Fig. 7, except that in the summer the mixed layer shallows to the 0.3 m depth level.

Comparison of water and ice speed with the three sets of boundary conditions are shown in Fig. 12. The period of September–December was chosen for a detailed comparison. The ice and water speed follow each other in time with the water speed showing a lesser amplitude in general. (Water speed is calculated on the first grid point at 0.3 m.)

In general, the ice speed (solid line) and water speed (dashed line) show phase agreement that reflects the inertial motion. Incorporation of the constant flux and molecular sublayer results in a lowering in water velocity magnitude as compared to the drag law. The water and ice phase agreement is similar to the drag law with some reduction in water velocity maxima.

For an illustrative comparison of ice and water speed against data, we picked the boundary conditions that incorporated an analytical representation of the constant flux and molecular sublayers. Figures 13 and 14

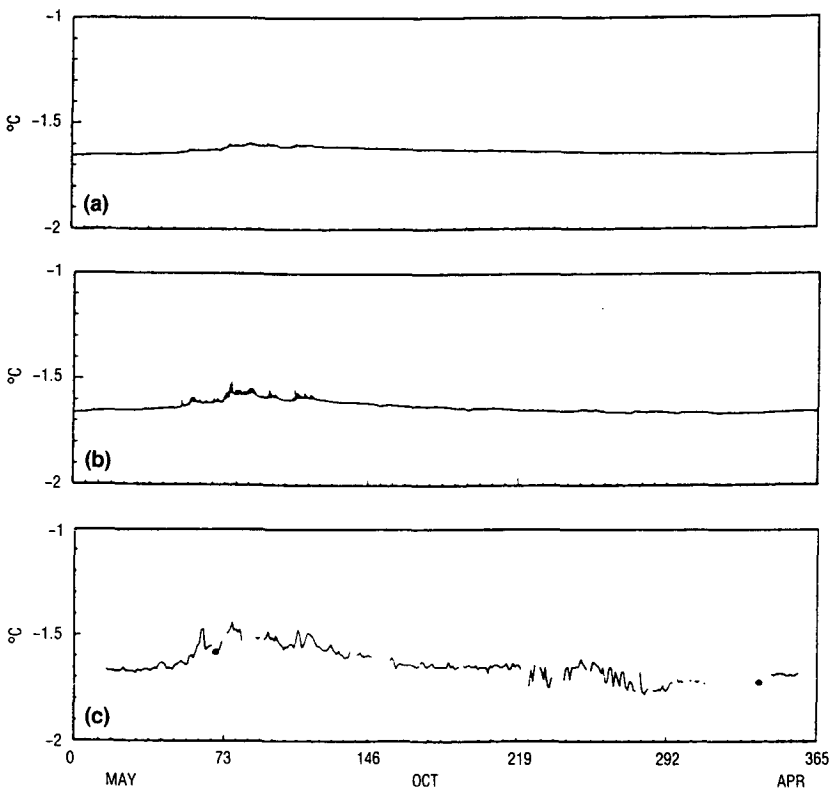


FIG. 10. Comparison of model simulated mixed-layer temperature with differing boundary conditions. (a) Results with constant flux layer applied to the temperature, salinity and momentum equations, (b) results with molecular sublayer applied to temperature, salinity, and momentum equations, and (c) data obtained at Station Snowbird.

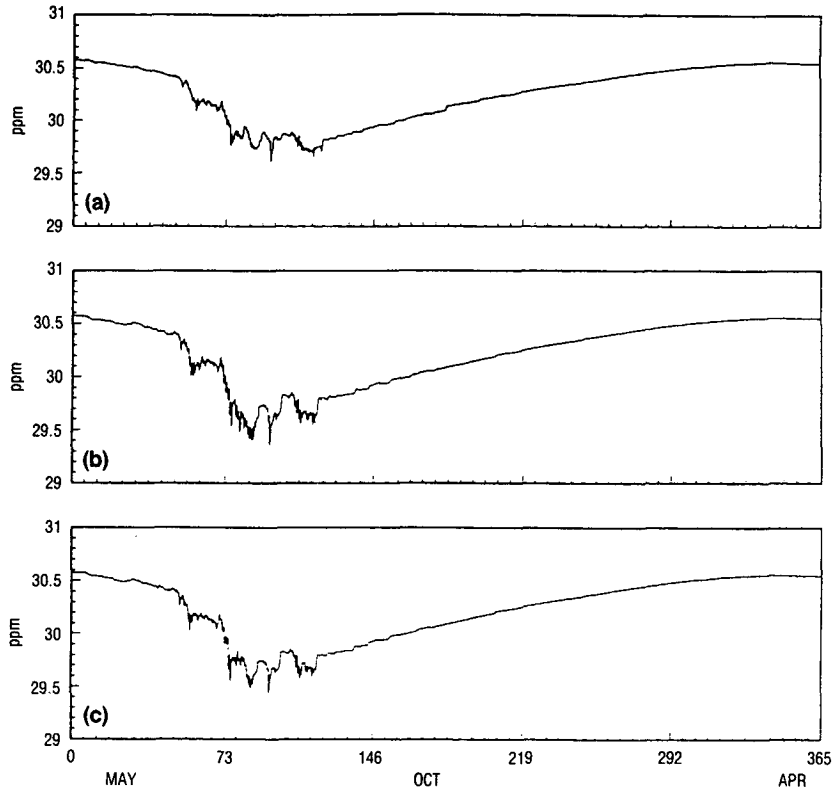


FIG. 11. Comparison of model simulated mixed-layer salinity with differing boundary conditions. (a) Results with constant flux layer applied to the temperature and salinity equations and the drag law applied to the momentum equation, (b) results with molecular sublayer applied to temperature, salinity, and momentum equations, and (c) results with constant flux layer applied to temperature, salinity, and momentum equations.

show the results. As indicated, we used data from camps Snowbird and Blue Fox. The camps were initially separated by a few degrees and drifted apart and towards the North Slope during the experiment.

There is agreement with the data for the ice and water speed. In some cases the data from one camp fits better the simulations than data from the other camp. In some cases the simulated speeds are less in magnitude than the data from either camp. Overall, the model simulations all show skill in amplitude and phase.

The atmospheric forcing used here represents an average condition in the region of the ice camps. The model neglects the internal ice stresses. We expect the internal ice stress to contribute to the ice rheology as the ice camps drift towards the North Slope and the ice is piled up.

In general, we find that the three sets of boundary conditions show agreement in simulated gross features such as velocity, temperature, and salinity. Differences arise in fine details of the boundary layer such as temperature and salinity fluctuations below the ice.

## 6. Conclusions

A coupled one-dimensional ice–ocean model was developed and used for studies of Arctic phenomena. One of Semtner's climatological studies was repeated and compared with our ice–ocean simulation. Semtner's simulation yielded a 6-year cycle of open water. Our model, with the same forcing and initial conditions, yielded open water nearly every year. This illustrates the effect of coupled feedback between ice and ocean. In our ice–ocean model, the depth of the mixed layer varies in response to forcing. The exchange of heat between the ocean and the ice varies with the mixing and heat input from below. The heat exchange was the greatest when the mixed layer deepened and entrained warmer water from below.

Large temperature differences in the water column developed when several days of open water occurred. This was due to penetration of solar radiation into subsurface layers and the formation of a warm spot in the water column. As ice re-formed, the warm region diffused. The heat was often released in bursts, either

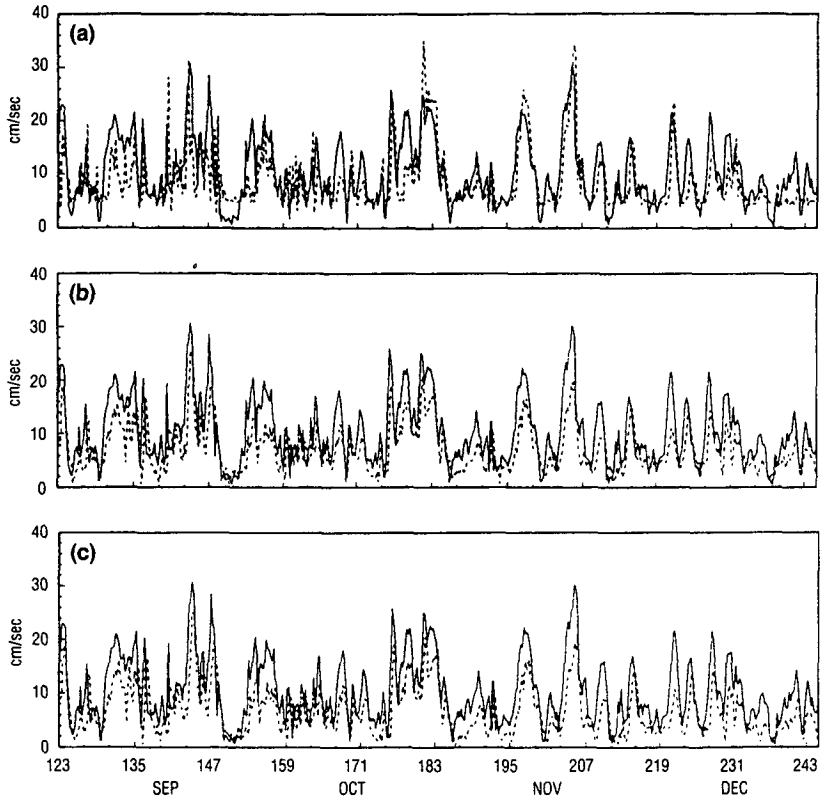


FIG. 12. Comparison of model simulated water speed (dashed line) and ice speed (solid line) with differing boundary conditions. (a) Results with constant flux layer applied to the temperature and salinity equations and the drag law applied to the momentum equation, (b) results with molecular sublayer applied to temperature, salinity, and momentum equations, and (c) results with constant flux layer applied to temperature, salinity, and momentum equations.

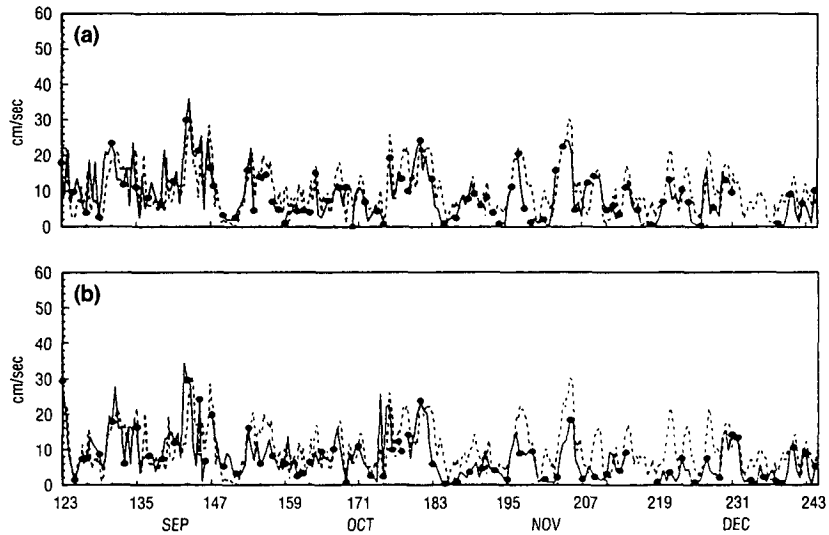


FIG. 13. Comparison of model simulated ice speed (dashed line) to data (solid line) from camp Snowbird (a) and camp Blue Fox (b) for the molecular sublayer case.

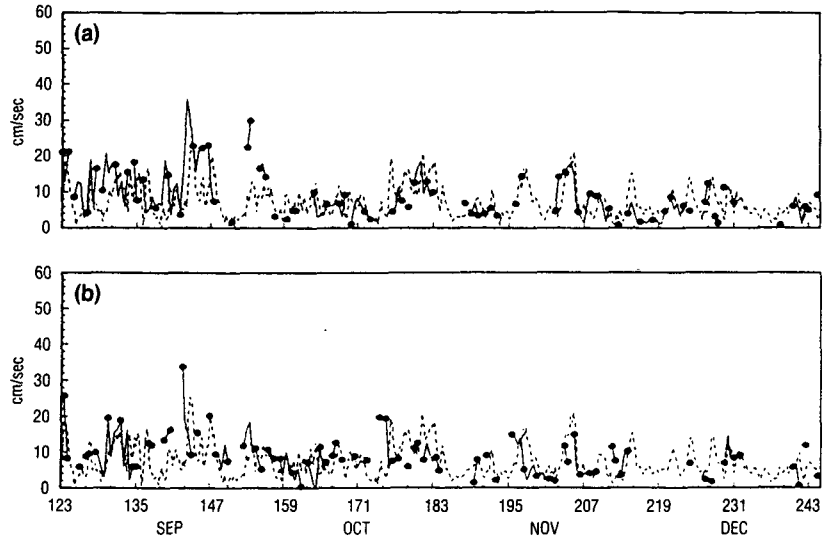


FIG. 14. Comparison of model simulated water speed (dashed line) to data (solid line) from camp Snowbird (a) and camp Blue Fox (b) for the molecular sublayer case.

slowing the freezing rate or melting a few centimeters of ice. The rate of heat release was controlled by salt flux and shear stresses.

The ice–ocean model was used to simulate the conditions of the AIDJEX experiment. The results of this simulation showed that the ice–ocean model simulated the general trends of the measurements. The model, however, did not reproduce some of the high variability observed in the ocean in the Beaufort Sea and underpredicted the deepening of the mixed layer. The omission of advection from the model is a primary reason for many of the discrepancies, since the temperature and salinity fields in the Beaufort Sea are perturbed by Pacific water, transit eddies, and the Beaufort Gyre. Other possibilities for the discrepancies were uncertainties in some of the forcing fields that control the thermodynamics, such as the snowfall and the heat input from the deep ocean. These forcing fields affect the growth of ice, which in turn affects the mixed-layer response.

We examined three different boundary conditions for temperature, salinity, and momentum. The constant flux and molecular sublayer representation showed some improvement in the variability of the mixed-layer temperature and salinity. The water and ice speeds showed qualitative and quantitative agreement with data for all boundary conditions. The mixed layer tended to shallow too much in all cases.

*Acknowledgments.* This work was sponsored by NORDAs basic research program 61153N. The AIDJEX data was provided by K. Hunk of Lamont–Doherty Geological Observatory. Dr. A. J. Semtner has provided valuable insight into the sensitivity of his multiyear ice simulations to various parameter.

## APPENDIX A

## Finite Difference Form of the Governing Equations

### 1. Ice velocity equation

We illustrate the solution of the ice momentum equations [Eqs. (1) and (2)] for the case where the stress between the ice and water is given by a drag law [Eqs. (19) and (20)]. The equation for the $x$-component of the ice velocity then becomes

$$\frac{\partial u_i}{\partial t} = f(v_i - v_g) + \frac{\tau_{ax}}{m} + 5.5 \times 10^{-3}\left[\frac{\rho_0}{\rho_i h_i}\right] \times [(u_g - u_i)^2 + (v_g - v_i)^2]^{1/2} \times [(u_g - u_i)\cos\theta - (v_g - v_i)\sin\theta] \quad \text{(A1)}$$

where $\theta = 25°$.

The equation for the $y$-component becomes

$$\frac{\partial v_i}{\partial t} = -f(u_i - u_g) + \frac{\tau_{ay}}{m} + 5.5 \times 10^{-3}\left[\frac{\rho_0}{\rho_i h_i}\right] \times [(u_g - u_i)^2 + (v_g - v_i)^2]^{1/2} \times [(v_g - v_i)\cos\theta + (u_g - u_i)\sin\theta]. \quad \text{(A2)}$$

Next, let $C = 5.5 \times 10^{-3}[\rho_0/\rho_i h_i][(u_g - u_i)^2 + (v_g - v_i)^2]^{1/2}$ and rearrange the terms in Eq. (A1) to get

$$\frac{\partial u_i}{\partial t} = (f + C\sin\theta)v_i - (C\cos\theta)u_i - fv_g + \frac{\tau_{ax}}{m} + Cu_g\cos\theta - Cv_g\sin\theta \quad \text{(A3)}$$

and in Eq. (A2) to get

$$\frac{\partial v_i}{\partial t} = -(f + C\sin\theta)u_i - (C\cos\theta)v_i + fu_g + \frac{\tau_{ay}}{m} + Cv_g\cos\theta + Cu_g\sin\theta. \quad \text{(A4)}$$

Let

$$F_x = -fv_g + \frac{\tau_{ax}}{m} + Cu_g\cos\theta - Cv_g\sin\theta, \quad \text{(A5)}$$

$$F_y = fu_g + \frac{\tau_{ay}}{m} + Cv_g\cos\theta + Cu_g\sin\theta, \quad \text{(A6)}$$

and

$$f' = f + C\sin\theta. \quad \text{(A7)}$$

Next, substituting Eqs. (A5), (A6), and (A7) into Eqs. (A3) and (A4) yields

$$\frac{\partial u_i}{\partial t} = f'v_i - (C\cos\theta)u_i + F_x, \quad \text{(A8)}$$

and

$$\frac{\partial v_i}{\partial t} = -f'u_i - (C\cos\theta)v_i + F_y. \quad \text{(A9)}$$

The finite difference form of the above equations is as follows:

$$\frac{u_i^{n+1} - u_i^n}{\Delta t} = f'v_i^{n+1} - (C\cos\theta)u_i^{n+1} + F_x^n, \quad \text{(A10)}$$

and

$$\frac{v_i^{n+1} - v_i^n}{\Delta t} = -f'u_i^{n+1} - (C\cos\theta)v_i^{n+1} + F_y^n. \quad \text{(A11)}$$

or

$$u_i^{n+1} = \frac{u_i^n + \Delta t f' v_i^{n+1} + \Delta t F_x^n}{1 + C\Delta t\cos\theta}, \quad \text{(A12)}$$

and

$$v_i^{n+1} = \frac{v_i^{n+1} - \Delta t f' u_i^{n+1} + \Delta t F_y^n}{1 + C\Delta t\cos\theta}. \quad \text{(A13)}$$

Solving Eqs. (A13) and (A12) for $u_i^{n+1}$ yields

$$u_i^{n+1} = \frac{(1 + C\Delta t\cos\theta)u_i^n + (1 + C\Delta t\cos\theta) \times \Delta t F_x^n + \Delta t f' v_i^n + \Delta t^2 f' F_y^n}{(1 + C\Delta t\cos\theta)^2 + \Delta t f'} \quad \text{(A14)}$$

The $y$-component of the ice velocity can now be found by substituting the value obtained for $u_i^{n+1}$ into Eq. (A13).

**2. Water velocity**

The momentum equations for the ocean [Eqs. (5) and (6)] are solved using a time-splitting technique. The $x$-component of the velocity is written as follows:

$$\frac{u_w^{n+1} - u_w^n}{\Delta t} = f\phi v_w^{n+1} + f(1 - \phi)v_w^n + \frac{\partial}{\partial z}\left[\frac{K_M(\partial u_w^n)}{\partial z}\right] - fv_g^n \quad \text{(A15)}$$

where $\phi$ can range from 0 to 1. In most simulations, $\phi = 1$ is used. The ambient diffusion $\nu$ is included in the $K_M$ term.

Next, solving Eq. (A15) for $u_w^{n+1}$ yields

$$u_w^{n+1} = u_w^n + \Delta t f\phi v_w^{n+1} + \Delta t f(1 - \phi)v_w^n + \Delta t\frac{\partial}{\partial z}\left[\frac{K_M\partial u_w^n}{\partial z}\right] - \Delta t f v_g^n. \quad \text{(A16)}$$

An intermediate value $u_w^*$ is assumed such that

$$\frac{u_w^* - u_w^n}{\Delta t} = \frac{\partial}{\partial z}\left[\frac{K_M\partial u_w^*}{\partial z}\right]. \quad \text{(A17)}$$

This equation can be solved for $u_w^*$ by using a tridiagonal solver.

Using this value of $u_w^*$, Eq. (A16) can be rewritten as

$$\frac{u_w^{n+1} - u_w^*}{\Delta t} = f\phi v_w^{n+1} + f(1 - \phi)v_w^n - fv_g^n, \quad \text{(A18)}$$

or

$$u_w^{n+1} = u_w^* + \Delta t f\phi v_w^{n+1} + \Delta t f(1 - \phi)v_w^n - \Delta t f v_g^n. \quad \text{(A19)}$$

In a similar fashion, the $y$-component of the velocity can be written as

$$\frac{v_w^{n+1} - v_w^*}{\Delta t} - f\phi u_w^{n+1} - f(1 - \phi)u_w^n + fu_g^n. \quad \text{(A20)}$$

and then as

$$v_w^{n+1} = v_w^* - \Delta t f\phi u_w^{n+1} - \Delta t f(1 - \phi)u_w^n + \Delta t f u_g^n. \quad \text{(A21)}$$

Finally, substituting Eq. (A21) into Eq. (A19) and solving for $u_w^{n+1}$ yields

$$u_w^{n+1} = \frac{u_w^* + \Delta t f\phi v_w^* - (\Delta t f)^2(1 - \phi)\phi u_w^n + \Delta t f(1 - \phi)v_w^n + (\Delta t f)^2\phi u_g^n - \Delta t f v_g^n}{1 + (\Delta t f\phi)^2}. \quad \text{(A22)}$$

The value for $v_w^{n+1}$ can be obtained by substituting the value computed for $u_w^{n+1}$ into Eq. (A21).

## 3. Parameterization of turbulent eddy fluxes

The turbulent eddy coefficients, $K_M$ and $K_H$, are given by the following equations

$$K_H = LqS_H, \tag{A23}$$

$$K_M = LqS_M, \tag{A24}$$

where $L$ is the turbulence length scale, $q$ is the square root of twice the turbulent kinetic energy, and $S_H$ and $S_M$ are stability functions that are a function of the gradient Richardson number Ri, where

$$\mathrm{Ri} = \frac{-\frac{g}{\rho_w}\frac{\partial \bar{\rho}}{\partial z}}{\left[\left(\frac{\partial \bar{u}}{\partial z}\right)^2 + \left(\frac{\partial \bar{v}}{\partial z}\right)^2\right]}. \tag{A25}$$

Here, $g$ is the acceleration of gravity and $\bar{\rho}$ is the mean-field density. The quantity $q$ is calculated from a form of the turbulent kinetic energy equation that expresses a local balance of shear production, buoyancy production, and viscous dissipation of turbulent kinetic energy. The equation is

$$LqS_M\left[\left(\frac{\partial \bar{u}}{\partial z}\right)^2 + \left(\frac{\partial \bar{v}}{\partial z}\right)^2\right] + LqS_H\left[\frac{g}{\rho}\frac{\partial \bar{\rho}}{\partial z}\right] - \frac{q^3}{15L} = 0. \tag{A26}$$

The turbulence length scale is calculated from the ratio of the first to the zeroth moment of the turbulence field (Mellor and Durbin 1975). Thus,

$$L = \frac{0.1\int_{-\infty}^{0} |z| q dz}{\int_{-\infty}^{0} q dz}. \tag{A27}$$

These equations along with Eqs. (7)–(10) close the turbulence parameterization.

## REFERENCES


Coachman, L. K. and K. Aagaard, 1974: Physical oceanography of arctic and subarctic seas. *Marine Geology and Oceanography of the Arctic Seas,* Y. Herman, Ed., Springer-Verlag, 1–72.

Fletcher, J. O., 1965: *The Heat Budget of the Arctic Basin and Its Relation to Climate.* The Rand Corporation, R-444-PR.

Hibler, W. D., 1980: Modeling a variable thickness sea ice cover. *Mon. Wea. Rev.,* **108**(12), 1944–1973.

——, and K. Bryan, 1984: Ocean circulation: Its effects on seasonal sea-ice simulations. *Science,* **224**(4648), 489–491.

Leavitt, E., M. Albright and F. Carsey, 1978: Report on the AIDJEX Meteorological Experiment, AIDJEX Bull. 39, Department of Oceanography, University of Washington/Seattle, 121–148.

Ledley, T. S., 1985: Sea ice: Multiyear cycles and white ice. *J. Geophys. Res.,* **90**(D3), 5676–5686.

Lemke, P., 1987: A coupled one-dimensional sea ice–ocean model. *J. Geophys. Res.,* **92**(C12), 13 164–13 172.

——, and T. O. Manley, 1984: The seasonal variation of the mixed layer and the pycnocline under polar sea ice. *J. Geophys. Res.,* **89**(C4), 6494–6504.

Maykut, G. A., and N. Untersteiner, 1969: *Numerical Prediction of the Thermodynamic Response of Arctic Sea Ice to Environmental Changes.* The Rand Corporation, RM-6093-PR.

Mellor, G. L., and T. Yamada, 1974: A hierarchy or turbulence closure models for planetary boundary layers. *J. Atmos. Sci.,* **31,** 1791–1806.

——, and P. A. Durbin, 1975: The structure and dynamics of the ocean surface mixed layer. *J. Phys. Oceanogr.,* **5,** 718–725.

——, M. G. McPhee and M. Steele, 1986: Ice–seawater turbulent boundary layer interaction with melting or freezing. *J. Phys. Oceanogr.,* **16,** 1823–1846.

Overland, J. E., H. O. Mofjeld and C. H. Pease, 1984: Wind-driven ice drift in a shallow sea. *J. Geophys. Res.,* **89**(C4), 6525–6531.

Parkinson, C. L., and W. M. Washington, 1979: A large-scale numerical model of sea ice. *J. Geophys. Res.,* **84**(C1), 311–337.

Pautzke, C. G., and G. F. Hornof, 1978: Radiation program during AIDJEX: A data rep., AIDJEX Bull. 39, Department of Oceanography, University of Washington, 165–185.

Pollard, D., M. L. Batteen and Y. Han, 1983: Development of a simple upper-ocean and sea-ice model. *J. Phys. Oceanogr.,* **13,** 754–768.

Riedlinger, S. H., and A. Warn-Varnas, 1987: Predictions and studies with a one-dimensional ice/ocean model. Naval Ocean Research and Development Activity, Stennis Space Center, MS 115. [NORDA Rep. 195]

Semtner, A. J., 1976: A model for the thermodynamic growth of sea ice in numerical investigations of climate. *J. Phys. Oceanogr.,* **6,** 379–389.

Untersteiner, N., 1964: Calculations of temperature regime and heat budget of sea ice in the central Arctic. *J. Geophys. Res.,* **69,** 4755–4766.

Yaglom, A. M., and B. A. Kader, 1974: Heat and mass transfer between a rough wall and turbulent fluid flow at high Reynolds and Peclet numbers. *J. Fluid Mech.,* **62,** 601–623.